

A new method of computation of current distribution maps in bulk high-temperature superconductors: analysis and validation

M Carrera¹, J Amorós², X Obradors³ and J Fontcuberta³

¹ Dep. Medi Ambient i Ciències del Sòl, Universitat de Lleida, Jaume II, 69. 25001 Lleida, Spain

² Dep. Matemàtica Aplicada I, Universitat Politècnica de Catalunya, Diagonal 647, Barcelona, Spain

³ Institut de Ciència de Materials de Barcelona, CSIC, Campus UAB, 08193 Bellaterra, Spain

E-mail: mcarrera@macs.udl.es and xavier.obradors@icmab.es

Received 28 May 2003, in final form 28 July 2003

Published 27 August 2003

Online at stacks.iop.org/SUST/16/1187

Abstract

We present a test and analysis of our method of computation of the distribution of currents in bulk superconducting samples, which is sensitive to current contribution in the deep layers of the sample. The procedure is based on measurements of the magnetic field with a Hall probe, inverted by linearization and orthogonal triangularization, known as QR decomposition, of the matrix in the resulting linear system. No assumptions on the number or geometry of domains are required. The only constraint on the method is that the critical current must be homogeneous along the c -axis. Our method is applied to real 3d samples with size in the cm range and different geometries of technological interest. The propagation of errors in the general case is analysed, and we also supply a method to estimate the error in every computation, which is applied to the computed $\mathbf{J}(J_x, J_y)$ in the above samples.

(Some figures in this article are in colour only in the electronic version)

1. Introduction

The use of large YBCO melt-textured blocks in practical applications requires a detailed understanding of current patterns. Many previous works have dealt with the inversion problem to obtain current maps from spatially resolved induction measurements. The first relevant works were based on models which assumed cylindrical symmetry for the samples and the current distribution [1–3]. Afterwards, Grant *et al* [4] developed a model for square-section thin films based on the discretization of the magnetization on a 2d grid over the sample, while Xing *et al* [5], and Kamijo and Kawano [6] used a computation methodology based on the linearization and matrix inversion which was applied to 2d samples. Keeping the planar approximation to the distribution of current, extensions were made to 3d samples: Zeisberger *et al* [7] used a fitting

procedure for the determination of an effective current density where axially symmetric current distribution is assumed; Wijngaarden *et al* [8, 9] and Joos *et al* [10] applied Fourier transform to magneto-optical flux measurements; finally, Amorós *et al* applied the well-known QR decomposition by Householder hyperplane reflection [11] to melt-textured bulk samples [12–14]. Moreover, Portabella *et al* [15] solved the inversion problem by a finite-element procedure that may be applied to 3d samples without any regularity assumption, but with important computational requirements.

In the present work we report further analysis of the current distribution computation following our linearization procedure of [12–14]. An analysis discussing the sources of error in the computation and its bounds is made. It is not possible to give a realistic universal error bound, but we

provide a method to check *a posteriori* the margin of error for every computed sample. To establish the capabilities and limitations of our method, we first apply it to simulated samples where we can compare the computed and original current circulations and make the possible sources of error evident. We proceed then to apply our method to real bulk samples with different geometries of practical interest, namely cylinders, rings and a rectangular prism with an artificial welding.

We show that the calculation procedure can be validated in two independent ways: (i) by direct computation of the field B_z induced by our calculated current, and (ii) by computation of the current from measurements of B_z at different heights above the sample. Our computation method is compared with that of [8–10], and it is found to provide a better validation and error control in bulk samples. Regarding the depth of resolution in calculated currents, the procedure of [8, 9] applied to magneto-optical imaging is mainly sensitive to the currents in a surface layer of $\sim 20 \mu\text{m}$ [16], while we will show that our algorithm yields accurate computations on samples with thickness in the mm range.

2. The method of computation

2.1. Computational procedure

Our starting point is a 3d bulk sample of superconducting material with a critical current $\mathbf{J} = (J_x, J_y, J_z)$ through it that verifies two properties:

- (i) The current circulation is planar, that is $J_z = 0$.
- (ii) The critical current circulation is the same on every horizontal layer, that is, the functions J_x, J_y depend only on x, y and the sample has a shape $A \times I$ where A is an arbitrary planar region and I an interval on the z -axis.

We do not make any assumption on the geometry of the planar current of the sample, its number of domains, their shape or extension. The procedure we apply to compute the critical current is a refinement of that of [5] for computing \mathbf{J} in 2d samples. As the current \mathbf{J} is planar, the vertical magnetic field at a point $\mathbf{r} = (x, y, z)$ around the sample is given by

$$B_z(x, y, z) = \frac{\mu_0}{4\pi} \int_{A \times I} \frac{3M(\mathbf{r}')((z - z')^2 - |\mathbf{r} - \mathbf{r}'|^2)}{|\mathbf{r} - \mathbf{r}'|^5} dV \quad (1)$$

where $\mathbf{r}' = (x', y', z')$ covers the sample with vertical symmetry $A \times I$ and $M(\mathbf{r}') = M(x', y')$ is the vertical magnetization. If we cover the base A with a fine rectangular *discretization grid* and we assume that the magnetization has a constant value $M(i, j)$ on the prisms $\Delta_{ij} \times I$ over every rectangle of the grid, formula (1) for the vertical magnetic field at a point (x_m, y_n, h) above the sample becomes a linear equation on the unknowns $M(i, j)$:

$$B_z(x_m, y_n, h) = \sum_{i,j} M(i, j) \frac{\mu_0}{4\pi} \int_{\Delta_{ij} \times I} \frac{3z^2 - r^2}{r^5} dV \quad (2)$$

where $r = |(x_m, y_n, h) - (x, y, z)|$, and the sum is taken over all rectangles in the discretization grid. Therefore, the values of B_z on a rectangular measurement grid over the sample containing enough points yield a determined or

overdetermined linear system that determines the discretized magnetization M . As discussed below, propagation of errors forces us to use overdetermined systems. The current $\mathbf{J} = \nabla \times M$ may then be estimated by numerical computation with a finite difference scheme. Thus the crux of the computation is the resolution of an overdetermined linear system, with $m \times n$ equations, the size of the *measurement grid*, and $m' \times n'$ unknowns, and the size of the discretization grid on which M is allowed to vary.

2.2. Sources of error

The possible error sources in the above computation of the magnetization M are the following:

- (i) The discretization error arising from the assumption that M is constant on the rectangles Δ_{ij} .
- (ii) Errors in the measurement of B_z , such as background noise.
- (iii) Errors in the numerical computation of the linear system coefficients $M(i, j)$, which are defined by equation (2).
- (iv) Rounding errors in the resolution of the linear system.

The absolute error incurred by replacing $M(x, y)$ with the constant $M(i, j)$ over every rectangle Δ_{ij} is bounded by $\|DM\|_\infty \text{diam } \Delta_{ij}$ where $\|DM\|_\infty$ is the maximal value of the norm of the differential of M on the rectangle Δ_{ij} and $\text{diam } \Delta_{ij}$ is the maximum distance between two points of Δ_{ij} . The norm $\|DM\|_\infty$ is the density of the current inside a current domain but may go to infinity at its edges: this reflects that a discretization procedure blurs the boundaries between domains of current or the sample and the exterior as rectangles Δ_{ij} overlap the two domains. The computation of J by numerical differentiation over the grid extends this error to neighbouring grid elements, resulting in an apparent widening of the current domains. We will refer to this as *domain overspill error*, and use a differentiation scheme for J to contain it within a margin of two elements of the discretization grid around every domain of current. Domain overspill errors become smaller with finer discretization grids for the magnetization M , but this refinement is limited by the relative error in the measurement of B_z that we proceed to discuss.

The magnetic field measurement error $\|\Delta B_z\|/\|B_z\|$ is the relative error with which the vertical magnetic field B_z is known at the measurement grid. It propagates from the independent term B_z to the solution M of the linear system (2). A bound for the global relative error $\|\Delta M\|/\|M\|$ is given by the formula

$$\frac{\|\Delta M\|}{\|M\|} \leq N \frac{\|\Delta B_z\|}{\|B_z\|} \quad (3)$$

where M (respectively B_z) are the vectors formed by all values of the magnetization M (field B_z), and the factor N is the *condition number* of the linear system (calculated as seen in [11]). The inverse $1/N$ of the condition number may be interpreted as the ‘amount of magnetic field signal’ that we are receiving at the measurement points of B_z from each element in the discretization grid. It behaves accordingly: (a) N grows at least exponentially with the height between the surface of the sample and the measurement points of B_z , (b) N grows sublinearly with the thickness of the sample and, (c) N increases strongly, albeit in a complex way, with the inverse of

the area of grid elements Δ_{ij} . Properties (a) and (b) are caused by the scattering of the received ‘magnetic field signal’: the magnetic field lines scatter widely above the sample, and much less inside it if the sample is at all homogeneous. Property (c) is an interference problem: as we subdivide the sample into smaller pieces, not only does each of them send a smaller amount of ‘magnetic field signal’ but, far worse, the signals from neighbouring pieces become very similar and interfere with each other.

The growth of the error factor N with the resolution of the grid of computation is a difficulty that arises with any scheme for computing \mathbf{J} based on a linearization of the problem, and imposes a limit on the spatial resolution of the calculated current distribution by any such linearization scheme. The limit depends in practice on the spatial resolution of the measured B_z , the geometry of each sample, the height at which the magnetic field has been measured over it, and the details of the linearization scheme. Once a discretization procedure has been selected, the resolution of the resulting linear system by QR decomposition is the method that will produce the smallest possible condition number among all resolutions [11]. For this reason, our method yields the smallest possible propagation of error from the measured B_z to the computed M and J among all schemes that assume discretization of M .

The error in the computation grows in the final step from M to the current J . To minimize the above-mentioned domain overspill errors we employ a four-point differentiation scheme computing \mathbf{J} at the centre of each grid element from the values of M at the four corners. The relative error of the computed current J has two components: (a) the error induced by the discretization of M on a grid, which is negligible as it is bounded by the third-order differential D^3M that is close to zero in regular domains, and (b) what we will call the *scintillation error*, which consists in that the variation of the error term ΔM between two neighbouring points of the grid may be larger than that of the correct function M and become the main term in their difference. There is no *a priori* bound for this type of error, which usually arises from scintillation in the measure of B_z , that gets multiplied by the condition number in M . As the magnetization M is very smooth, this error is greatly reduced with little loss of accuracy by interpolating the function M at the midpoints of the grid cells as the average of the values at the corners, but even after this there is no universal bound for the error in the resulting \mathbf{J} , and it has to be estimated for every sample by comparing the measured magnetic field B_z with the field that the computed \mathbf{J} would induce.

Finally, the errors introduced in the computation of the coefficients of the resulting linear system and in its resolution may be made arbitrarily small as these computations can be carried out with arbitrary accuracy. The efficient approach is to arrange the accuracy in the computation of the system coefficients so that its margin of error is small compared to the measure error $\|\Delta B_z\|/\|B_z\|$.

3. Validation of the method in simulated samples

We have tested our computation methodology on a variety of simulated samples where the current distribution \mathbf{J} is originally known. An additional advantage of these simulated samples is that the magnetic field \mathbf{B} may be computed to

Table 1. Computation parameters for the calculated M and J in the simulated sample 1.

Grid size (mm)	Factor N	$\ \Delta M\ /\ M\ $ (%)
0.40×0.40	5	0.05
0.25×0.25	24	0.24
0.15×0.15	400	4

any desired accuracy (no measuring errors), and it may be perturbed in a controlled way. The standard test on a simulated sample has been to fix a geometry for the sample, prescribe a current circulation \mathbf{J} through it, compute the vertical magnetic field B_z that \mathbf{J} induces on a ‘measurement’ grid over the sample by numerical integration of the Biot–Savart equation, and afterwards to compute the current distribution with our programme and compare it with the original current.

We have limited this section to two simulated samples that resemble the experimental ones in section 4, but we have also verified the capability of our method to compute current maps in the cases where the circulation of current or even geometry of the sample is highly asymmetrical (such as multiple domain samples, or rectangles with a non-centro-symmetric drilled hole [17]).

3.1. Partially penetrated state in a cylinder

The first simulation, in which we will discuss the limits to the resolution of our current maps, is a cylindrical sample with two opposing concentric rings of current, but such that they cover only the outer strip of the cylinder. This is the situation expected from the critical state model in superconducting samples that have been subjected to a maximum magnetic field that is smaller than their penetration field H^* and then lead to the remnant state. We have considered the cylindrical sample with diameter 11.4 mm and thickness 3 mm (as someone of our real samples) where the opposing rings occupy strips of width 1.25 mm each. The density of current is 8000 A cm^{-2} in each ring.

We have computed the vertical magnetic field B_z at a height of 0.5 mm on a 0.15×0.15 mm grid, with relative error $\|\Delta B_z\|/\|B_z\| < 10^{-4}$. Our method for the inverse computation has been applied three times to this grid of values of B_z , computing the current distribution $\mathbf{J}(x, y)$ with three resolutions of increasing fineness. Table 1 presents the size of the grids for M and J , the condition number of the computation, and the relative error in the computed M .

Figure 1 illustrates the capabilities and limits in the resolution of current density maps $J(x, y)$: the three computations approximately yield the correct density of the current and the delimitation of its rings. The computation with a resolution of 0.4×0.4 mm yields a very precise value for the density of J , but the obtained rings are about 1 mm too wide on the inner side. This is an instance of the domain overspill error induced by the assumption of discreteness of the current; it is proportional to the size of the grid elements. The computation with the maximal resolution of 0.15×0.15 mm minimizes this overspill error, but its high condition number results in a background oscillation noticeable both on the current rings and in the empty inner core. The computation of $J(x, y)$ with a resolution of 0.25×0.25 mm turns out for this sample to be

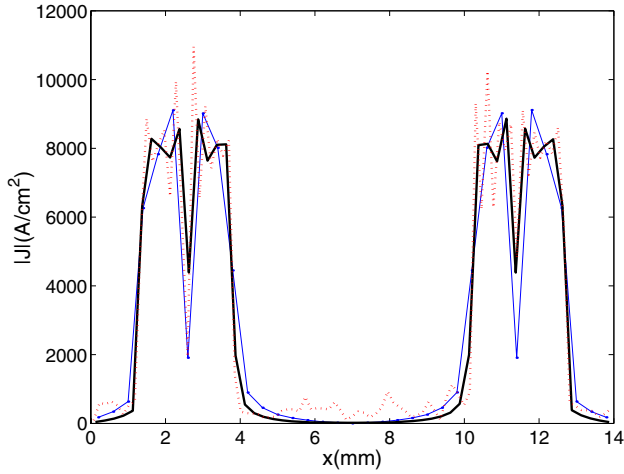


Figure 1. Simulated sample 1. Absolute value of calculated current density profiles along the x -axis at a value of the y -axis that corresponds to the centre of the sample. Narrow line (blue): 0.4×0.4 mm grid, wide line (black): 0.25×0.25 mm grid, dotted line (red): 0.16×0.15 mm grid.

the optimal compromise between the overspill error and that passed from B_z via the condition number.

The resolution with which the current J may be computed is proportional to the dimensions of the sample. Moreover it depends on its geometry, with thin films yielding better resolution than bulks, and on the height of measure of B_z , as we proceed to show.

3.2. Fully penetrated state in a cylinder

We will discuss the influence of the height of measurement of B_z with our second simulation. This is a cylindrical sample, with the same geometry as the previous one, covered by two opposing concentric rings of current with uniform density $J = 8000$ A cm $^{-2}$. Such is the current distribution expected from a critical state model in superconducting samples that have been subjected to a maximum magnetic field equalling their penetration field H^* and then removing it, i.e. the superconducting sample stays in the remanent state.

We have computed the vertical magnetic field B_z on 0.15×0.15 mm grids at heights $z = 0.5$ to 2.5 mm with 0.5 mm intervals, and a relative error bound $\|\Delta B_z\|/\|B_z\| < 10^{-4}$. Our method for the inverse computation of the current distribution has been applied to each of these grids with a fixed resolution of 0.4×0.4 mm for the magnetization M and current density J .

In figures 2 and 3 we show the resulting J from the field B_z at $z = 0.5$ mm. Note the excellent agreement between the original and the computed current inside the rings. The only noticeable difference between the two currents is the overspill at the boundaries of the current rings: the two rings of current in the computed J are separated ~ 1 mm, the computed outer boundary of the sample has advanced about 0.5 mm with respect to the original boundary, and a drop in the current density with diameter of about 1 mm appears at the centre. These are the boundary blurring (or domain overspill) errors mentioned in section 2.2, note that their width is about one discretization step on each side of the boundary.

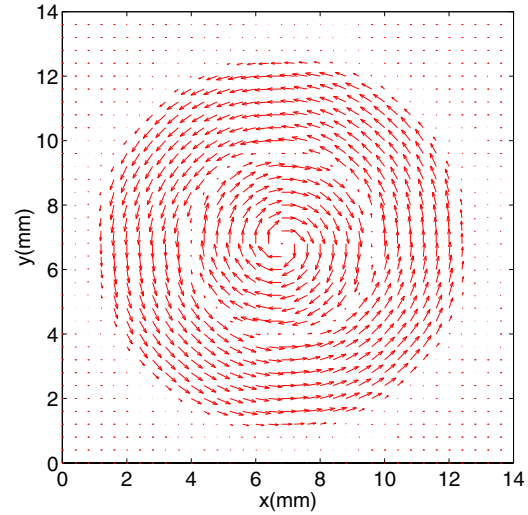


Figure 2. Simulated sample 2. Circulation of current vectors calculated from inversion of the magnetic field at $z = 0.5$ mm.

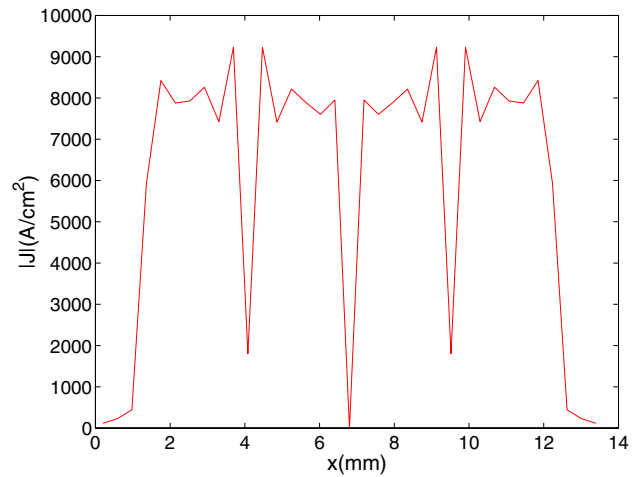


Figure 3. Simulated sample 2. Calculated current density profile (absolute value) that corresponds to the section along the x -axis at central value y in figure 2.

Table 2. Simulated sample 2. Condition numbers and relative errors in the magnetization M at different heights from which the magnetic field was inverted.

Height (mm)	Factor N	$\ \Delta M\ /\ M\ $ (%)
0.5	5	0.05
1	91	1
1.5	2 322	23
2	63 700	637

Table 2 shows the condition numbers and relative errors in the magnetization M at the different heights. While the domain overspill is determined by the grid size and is the same for all heights, the increase with the height of the condition number, thus of the relative error in M , J , is so great that, while it is negligible up to $z = 1$ mm, it is comparable with the value of M at $z = 1.5$ mm and dominates over the real value for $z > 1.5$ mm. In fact, if the margin of error of our values of B_z had been typical of real measurements ($\Delta B_z \sim 0.2$ G) even at a height of 1 mm this error would have had noticeable effects.

This exponential (at least) growth of the condition number is caused by the increase of the height of measurement of the field B_z .

3.3. Assessment of the simulations

The coincidence of the computed current with the original one away from the boundaries of current domains in all the reported simulations demonstrates that the numerical errors in the computation of the coefficients of the linear system and in its resolution are negligible.

The first simulated example showed the ability of our algorithm to distinguish spatially variable features of the current circulation, and the limit to its resolution in the absence of error in the magnetic field B_z . Comparison with the experimental samples of the following section will prove that this error in the measurement of B_z is the main source of error in computations from real experimental data.

The second simulation shows that, to achieve the least global error in $\mathbf{J}(x, y)$ in a sample homogeneous along the c -axis, the magnetic field should be measured as closely above the sample as possible, because of the extraordinary growth of the error factor measured by the condition number of the system, which multiplies the error in the experimental measurement of B_z .

If the sample is a bulk one and it is unknown whether it is homogeneous along the c -axis, the computed distribution of J has a margin of error that is possibly uneven in the different vertical layers of the sample, and always increasing with their depth as the magnetic field B_z measured above the sample is mostly induced by the current in the upper layers. Nevertheless, the contribution of the bottom layers of the sample to the magnetic field B_z above it varies very little while the height of measurement is small compared to the thickness of the sample. For instance, in a cylinder with diameter 1 cm and thickness 3 mm with a current that is homogeneous in z the contribution of the bottom 50% of the sample to the measured magnetic field is 30% at a height of 0.5 mm, and 27% at a height of 5 μm . Thus the global margin of error of J for the lower half of the bulk sample goes from 2.33 to 2.70 times that in its upper half.

Consequently, the optimal height of measurement of B_z is the smallest possible, as the loss of information about the deep layers of the sample is far outweighed by the smaller propagation of the measurement error $\|\Delta B_z\|/\|B_z\|$ through the condition number. We remark by the way that although the margin of error grows with depth our procedure yields relevant information about all layers of the bulk sample.

4. Validation of the computational method in experimental samples

The ultimate validation of our computation algorithm, and the test of its limitations, will result from its application to real experimental measurements obtained in samples with diverse geometries of technological interest, such as cylinders, parallelepipeds or rings. Also the influence of the thickness and the height of the measurement should be investigated. In the following sections we analyse magnetic field distributions measured in samples of bulk melt textured $\text{YBa}_2\text{Cu}_3\text{O}_7$

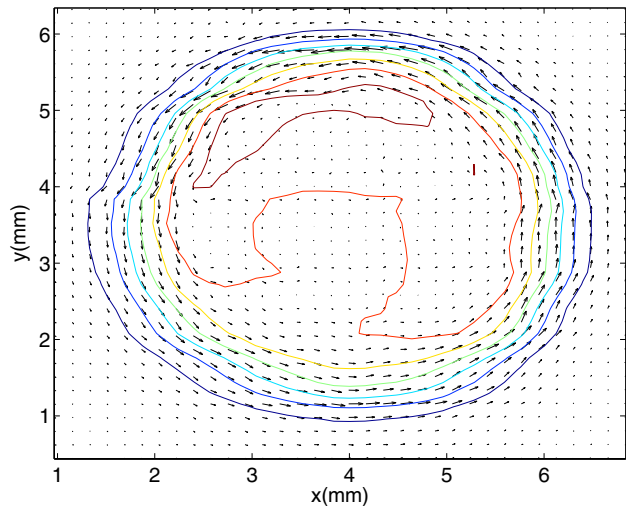


Figure 4. Level curves of remanent flux distribution after a FC process superposed with circulating current vectors calculated from a flux map.

(YBCO). Examples of cylindrical and rectangular samples have been widely discussed previously [12, 14, 18].

4.1. Distribution of currents in a ring-shaped sample

A ring-shaped sample of YBCO was obtained by drilling a disc of single domain melt textured pellet that was grown by top seeding growth following processes previously described [16, 19]. The size of our sample is: 4.9 mm of external diameter and 3.25 mm of inner diameter, and the thickness of the sample is 0.65 mm. In this case the Hall probe measurements were carried out using an in-field magnetic imaging system described previously [20]. The external magnetic field is applied perpendicular to the surface of the sample and the Hall probe (active area $0.1 \times 0.1 \text{ mm}^2$) is rastered, maintaining a flying distance between 80–100 μm over the polished surface of the sample, in steps of 160 μm .

Figure 4 shows the level curves of the measured magnetic field $B_z(x, y)$ in the remanent state after a FC process under an applied field $H_{\text{ap}} = 2.2 \text{ kOe}$. Note the global homogeneity of the distribution of the trapped field, with a maximum of 328 G, and the local asymmetries, some of which are caused by irregularities in the geometry of the ring and others due to microstructural sample inhomogeneities. The current has been computed with a resolution grid of $0.18 \times 0.18 \text{ mm}$. A height of probe of 80 μm has been assumed, and the resulting condition number is 1.44, which is highly satisfactory. With the selected resolution the circular band has a width of five elements of the $B_z(x, y)$ grid, and four elements of the computation grid for $J(x, y)$. Figure 4 depicts superposed onto the magnetic field distribution lines the circulation vectors of the critical current density. Note the agreement between the vector field and the level sets for B_z .

Figure 5 shows cross sections of the modulus of critical current density $J(x, y)$, at the orthogonal diameters given by $x = 3.90 \text{ mm}$ and $y = 3.21 \text{ mm}$ in figure 4. The cross section at constant y is symmetric and has maximum value around $1.1 \times 10^4 \text{ A cm}^{-2}$, while the section at constant x has an asymmetry with a density peak of $1.6 \times 10^4 \text{ A cm}^{-2}$ on the right side

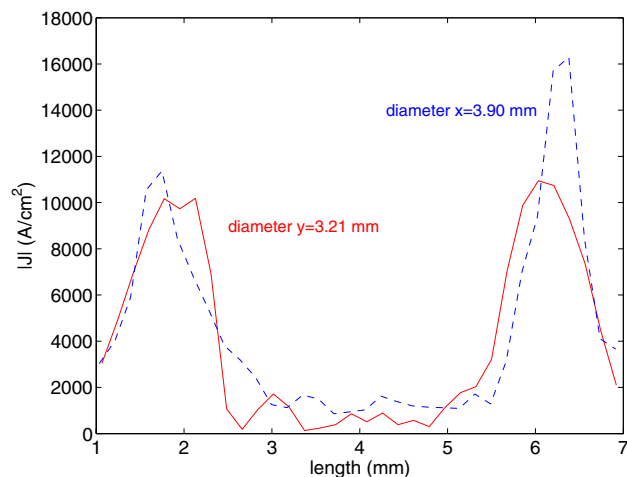


Figure 5. Calculated current density profiles (absolute value) that correspond to two orthogonal sections at the indicated positions with respect to figure 4.

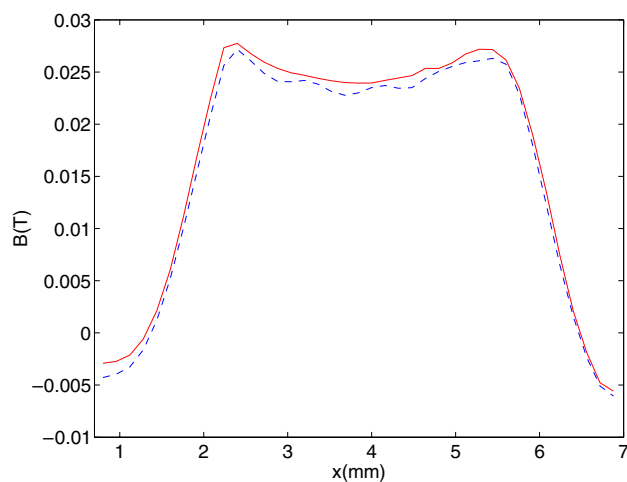


Figure 6. Measured (continuous line) and calculated (dotted line) B_z profiles. The profiles correspond to the section along the x -axis at a central value of the y -axis ($y = 3.36$ mm in figure 4).

corresponding to the upper side region of the ring in figure 4. The width of the computed band of current agrees with the real width of the ring up to the margin of error theoretically expected, about one element of the computation grid on each edge.

Due to the uncertainty about the height of the Hall probe we have performed the computation of the current with varying heights in the 80–100 μm range. The global critical current only increases by $\sim 1.75\%$ between these heights, and the peak value of its density by 7.5%. Figure 6 shows the comparison of the originally measured magnetic field B_z and that induced by our computed current. The discrepancy between the two fields is less than 6% inside the sample.

The calculated critical current density using a critical state model from magnetization hysteresis loops measured with the SQUID magnetometer in similar rings was $J_c = 2.8 \times 10^4$ A cm^{-2} . So, our calculated values are in rather good agreement with those.

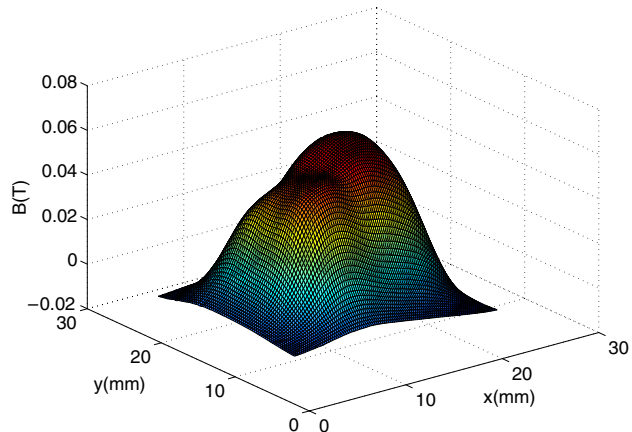


Figure 7. Remanent flux map measured after a FC process.

4.2. Distribution currents in a rectangular-shaped sample

The second example corresponds to samples that were obtained from a YBCO cylinder ($\varnothing = 35$ mm, $h = 25$ mm) fabricated with directional solidification in a temperature gradient, in which the influence of the processing parameters on the microstructure and the levitation and flux trapping properties were studied [13].

Two parallelepiped blocks have been cut from the same cylinder. The larger one, with a section of 14.3×12.6 mm and thickness of 6.3 mm, had a typical multidomain structure. The other one, with a section 10×8.5 mm and thickness of 4 mm, presents a monodomain structure.

Remnant magnetic flux measurements were performed using a SmCo magnet ($\varnothing = 25$ mm, $h = 20$ mm) with $B_r = 0.33$ T. A Hall microprobe was scanned at 1 mm from the surface after a field cooling, with a resolution of 0.2×0.25 mm. The resulting mapping is displayed in figure 7, where the irregularity of the distribution induced by the existence of several domains is clearly seen. The maximum remnant field is 653 G.

The critical current has been computed with a 0.47×0.61 mm resolution. The condition number of the computation was 22.5. The increase in this error factor and coarsening of the current map (figure 8) compared to the previous examples is mainly due to the greater height at which the field B_z has been measured. Nevertheless, the computed current circulation still reflects the inhomogeneities in the sample. The distribution of current density distinguishes a region with density around 7000 A cm^{-2} , and another region on the opposite side of the sample with density below 3000 A cm^{-2} . The above-cited monodomain sample had a maximum remnant field of 750 G, and the computation of its critical current resulted in a homogeneous distribution, with a maximum of around 7000 A cm^{-2} . Note thus the concordance of both computations, and how they suggest that only one side of the irregular sample maintains the quality of the monodomain sample.

4.3. Distribution currents in an artificially welded sample

Experimental characterization methods for the study of artificial welding of melt-textured YBCO blocks have become

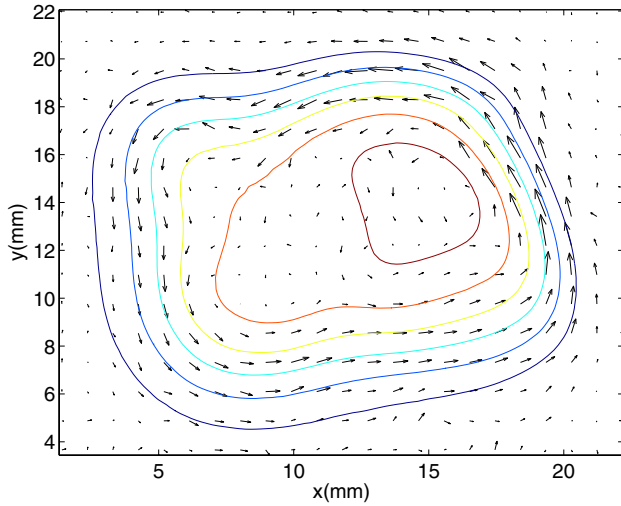


Figure 8. Circulating current vectors calculated from flux mapping of figure 7. Superposed are the level curves of that flux map.

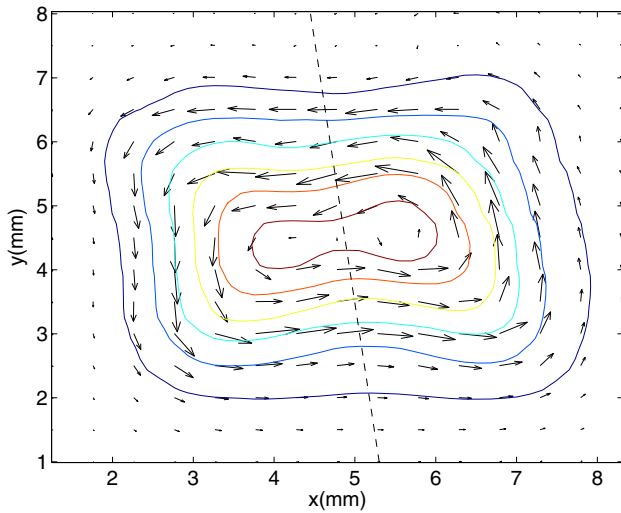


Figure 9. Level curves of remanent flux distribution after a FC process superposed with the circulating current vectors calculated from this flux map. The dotted line indicates the approximate position of the welding.

of utmost necessity in engineering devices where complex-shaped pieces are required. With this example we would like to illustrate how our inversion method allows us to determine the distribution and magnitude of local currents over the sample, and to evaluate the effects induced by the joining. So we may be able to separate different quality joints.

Our welding samples were obtained using a Ag surface melting induced welding technique following a process that is described in [21–26]. We discuss now results for a parallelepipedic sample of dimensions: $a = 5.6$ mm, $b = 5.23$ mm, and 4.92 mm of thickness. The joined plane is perpendicular to the ab -plane, across the shorter axis.

The Hall mapping system used is the same mentioned in the previous section, with a scanning over the ab -plane at a flying distance of $80 \mu\text{m}$ in steps of $160 \mu\text{m}$. The magnetic field distribution has been measured after a FC process, and reflects clearly the two domains induced by the partial entry of flux at the joint, as shown in figures 9 and 10. The maximum

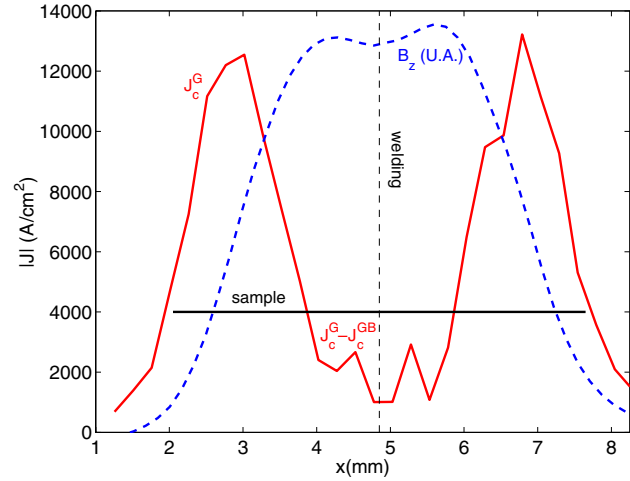


Figure 10. Absolute value of calculated current density profile (continuous line) in a section crossing the joining plane taking a position that corresponds to the centre of the sample ($y = 4.5$ mm in figure 9). The measured B_z profile (dotted line) is represented in arbitrary units. The horizontal line is only a reference indicating the sample dimension, and the vertical dotted line indicates the approximate position of the welding.

value of remanent field is 1080 G, decreasing around 5% in the minimum over the joint. Due to higher noise in the measurement of the field B_z , the current distribution has been computed with a resolution of 0.25×0.25 mm, which is coarser than that of example 4.1. The condition number of the resulting computation is 1.49.

Calculated current distributions of a good quality weld from a FC trapped field show a single circulation loop over the whole sample that is typically indistinguishable from that of a non-welded sample. In our case, from the calculated $J(x, y)$ we may infer the intergrain current J_c^{GB} and the intragrain current in each domain J_c^G . For greater clarity we show in figure 10 a profile of the density of current and measured magnetic field over a cross section orthogonal to the joining plane, which is marked out by the dent in the magnetic field. The two smaller central crests in the J profile correspond to the difference between loop currents $J_c^G - J_c^{GB}$, with a density of around 2800 A cm^{-2} . The larger outer crests correspond to the intragranular current, with a density of about 12500 A cm^{-2} . This implies that $J_c^{GB} \approx 9700 \text{ A cm}^{-2}$. The effect of the welding is thus evaluated by the quotient $J_c^{GB}/J_c^G \approx 77\%$. The current density modulus in cross sections parallel to the welding plane through the centre of each domain (not shown here) presents the unique loop corresponding to the intragranular current. Our calculated value of J_c^G is a typical value measured through inductive critical current density measurements in large domain melt processed YBCO [21, 27].

5. Conclusions

We have shown that the inversion procedure described here allows the evaluation of the critical current distributions in HTSC materials.

The novelty of our method lies in two basic aspects: first, we release from any symmetry-related condition the in-plane current distribution, and, second, we provide an accurate

estimate and control of the error in the computation of \mathbf{J} . This latter aspect is a critical problem in real samples, so we employ a QR inversion algorithm that gives the minimal propagation among linear schemes of the error from the measured B_z to the computed $\mathbf{J}(x, y)$.

The validity of the method has been illustrated by a number of tests and examples. We emphasize its sensitiveness to the current in the layers with depth in the mm range in the sample, even if the magnetic field B_z has been measured at heights in the μm range. This feature makes our procedure specially suitable for the computation of the critical current in bulk superconducting samples.

Acknowledgments

This work was supported by the Spanish CICYT (MAT99-0855-C02-01), and the Generalitat de Catalunya (2001-SGR-00336 and 2001-SGR-00334).

References

- [1] Frankel D J 1979 *J. Appl. Phys.* **50** 5402
- [2] Daümling M and Larbalestier D C 1989 *Phys. Rev. B* **40** 9350
- [3] Conner L W and Malozemoff A P 1991 *Phys. Rev. B* **43** 402
- [4] Grant P D, Denhoff M W, Xing W, Brown P, Govorkov S, Irwin J C, Heinrich B, Zhou H, Fife A A and Cragg A R 1994 *Physica C* **229** 289
- [5] Xing W, Heinrich B, Hu Z, Fife A and Cragg A 1994 *J. Appl. Phys.* **76** 4244
- [6] Kamiyo H and Kawano K 1997 *IEEE Trans. Appl. Supercond.* **7** 1228
- [7] Zeisberger M, Habisreuther T, Litzkendorf D, Müller R, Surzhenko O and Gawalek W 2002 *Physica C* **372–376** 1890.
- [8] Wijngaarden R J, Spoelder H J W, Surdeanu R and Griessen R 1996 *Phys. Rev. B* **54** 6742
- [9] Wijngaarden R J, Heeck K, Spoelder H J W, Surdeanu R and Griessen R 1998 *Physica C* **295** 177
- [10] Jooss Ch, Forkl A, Warthmann R and Kronmuller H 1998 *Physica C* **299** 215
- [11] Golub G and Van Loan C F 1989 *Matrix Computations* 2nd edn (Baltimore, MD: John Hopkins University Press)
- [12] Amorós J, Carrera M, Granados X, Fontcuberta J and Obradors X 1997 *Applied Superconductivity 1997 (Inst. Phys. Conf. Ser. 158)* (Bristol: Institute of Physics Publishing) pp 1639–42
- [13] Yu R, Mora J, Sandiumenge F, Vilalta N, Gomis V, Martínez B, Rodríguez E, Amorós J, Carrera M, Granados X, Camacho D, Fontcuberta J and Obradors X 1997 *IEEE Trans. Appl. Supercond.* **7** 1809
- [14] Mendoza E, Carrera M, Varesi E, Carrillo A E, Puig T, Amorós J, Granados X and Obradors X 2000 *Applied Superconductivity 1999 (Inst. Phys. Conf. Ser. 167)* (Bristol: Institute of Physics Publishing) p 127
- [15] Portabella E, Palka R, May H and Canders W R 2000 *Applied Superconductivity 1999 (Inst. Phys. Conf. Ser. 167)* (Bristol: Institute of Physics Publishing) p 1063
- [16] Joos Ch, Albrecht J, Kuhn H, Leonhardt S and Kronmüller H 2002 *Rep. Prog. Phys.* **65** 651
- [17] Carrera M, Amorós J, Obradors X and Fontcuberta J at press
- [18] Carrera M, Amorós J, Carrillo A E, Obradors X and Fontcuberta J 2003 *Physica C* **385** 539
- [19] Zheng H, Claus H, Chen L, Paulikas A P, Veal B W, Olsson B, Koshelev A, Hull J, Crabtree G W and Boyd G A 2001 *Physica C* **350** 17
- [20] Granados X, Sena S, Bartolomé E, Palau A, Puig T, Obradors X, Carrera M, Amorós J and Claus H 2003 *IEEE Trans. Appl. Supercond.* **13** 3667
- [21] Obradors X, Yu R, Sandiumenge F, Martínez B, Vilalta N, Gomis V, Puig T and Piñol S 1997 *Supercond. Sci. Technol.* **10** 884
- [22] Wiesner U, Krabbes G, Uelzen M, Magerkurth C, Plewa J and Altenburg H 1998 *Physica C* **294** 17
- [23] Nakamura Y, Tachibana K, Kato S, Ban T, Yoo S I and Fujimoto H 1998 *Physica C* **294** 302
- [24] Habisreuther T *et al* 2001 *IEEE Trans. Appl. Supercond.* **11** 3501
- [25] Chen L, Claus H, Paulikas A P, Zheng H and Beal B W 2002 *Supercond. Sci. Technol.* **15** 672
- [26] Iliescu S, Sena S, Granados X, Bartolomé E, Puig T, Obradors X, Carrera M, Amorós J, Krakunovska S and Habisreuther T 2003 *IEEE Trans. Appl. Supercond.* **13** 3136
- [27] Zheng H, Jiang M, Nikolova R, Welp U, Paulikas A P, Huang Y, Crabtree G W, Veal B W and Claus H 1999 *Physica C* **322** 1